Materials Today Communications 55 (2026) 115829

Contents lists available at ScienceDirect

Materials Today Communications

journal homepage: www.elsevier.com/locate/mtcomm

Prediction of doped silicon phases for enhanced lithium-ion battery anodes: Exploring the superior potential of C, N, and F doping

Samson Singo [a], Katlego Phoshoko [b], Tshidi Mogashoa [a], Phuti Ngoepe [a], Raesibe Ledwaba [a,*]

[a] Materials Modelling Centre, University of Limpopo, Private Bag x1106, Sovenga 0727, South Africa
[b] Data Intensive Research Initiative of South Africa, Council for Scientific and Industrial Research, P.O. Box 395, Pretoria 0001, South Africa

ARTICLE INFO

Keywords:
Silicon-based anodes
Lithium-ion batteries
High theoretical capacity
Volume expansion
Particle pulverization
Solid electrolyte interphase (SEI)
Cluster expansion

ABSTRACT

Silicon-based anodes are promising candidates for next-generation lithium-ion batteries owing to their high theoretical capacity, natural abundance, and environmental compatibility. However, their practical implementation is limited by severe volume expansion during lithiation and delithiation, resulting in particle pulverization, loss of electrical contact, and instability of the solid electrolyte interphase (SEI) layer. Doping has emerged as an effective strategy to mitigate these challenges and improve the structural and electrochemical performance of silicon anodes. In this study, the effects of carbon, nitrogen, and fluorine doping on silicon were investigated using the cluster expansion method. Several ordered phases, including SiC, SiF_2, SiF_5, SiN, SiN_2, and SiN_5, were predicted to be the most thermodynamically stable structures along the DFT ground-state line. SiN exhibited the most balanced overall performance, as indicated by thermodynamic, mechanical, and dynamical stability, along with semiconducting behaviour and a band gap of 1.76 eV. In contrast, SiN_2 displayed semimetallic conductivity and superior ductility (Pugh's ratio = 2.48, Poisson's ratio = 0.32), although phonon calculations indicated vibrational instability. Carbon doping produced the dynamically stable SiC phase with an enlarged band gap of 2.31 eV but increased brittleness, while fluorine-doped phases exhibited favourable electronic properties but poor mechanical and vibrational stability. The results demonstrate that dopant selection strongly influences the structural, electronic, mechanical, and vibrational properties of silicon, with nitrogen doping offering the most promising route for developing durable silicon-based lithium-ion battery anodes.

1. Introduction

The need for energy storage systems has risen significantly due to their role in optimising energy management and balancing energy supply with demand [1]. This increase follows the realization that renewable energy sources are often unreliable under non-ideal operating conditions, such as when solar panels are less effective in rainy weather. Moreover, there has been a global surge in energy demand due to rapid industrialization and technological progress in developing countries. Energy storage systems also serve to mitigate environmental issues caused by CO_2 emissions from traditional energy sources [1–3]. Lithium-ion batteries (LIBs), which are a type of rechargeable battery that can be cycled through charge-discharge processes, offer the advantages of high energy density and low self-discharge rate [4,5]. However, the low theoretical capacity of graphite-based LIBs (372 mAh/g) limits their ability to meet current energy demands, prompting research into alternative anode materials [6].

Silicon, the second most abundant element in the Earth's crust and a widely used semiconductor in the electronics industry, has shown great promise as a next-generation anode material for LIBs due to its high theoretical capacities of 4200 mAh/g ($Li_{4.4}Si$) and 3590 mAh/g ($Li_{3.75}Si$) [7]. Despite this promise, as the formation of Li-Si occurs, silicon goes through severe volume changes (>300%) that lead to pulverization of the silicon particles [8]. The severe volume expansion of silicon anodes originates from the lithiation-induced phase transformations that occur during battery operation [9]. During lithiation, crystalline silicon (c-Si) initially reacts with lithium to form an amorphous lithiated phase (a-Li_xSi), accompanied by a progressive loss of long-range crystalline order [10]. As lithiation proceeds, the lithium concentration increases until highly lithiated phases, approaching $Li_{15}Si_4$ at room temperature, are formed [9,10].

During delithiation, the reverse transformation does not fully restore the original crystalline silicon structure; instead, the material often remains in an amorphous state [10–12]. The repeated

* Corresponding author.
E-mail address: raesibe.ledwaba@ul.ac.za (R. Ledwaba).

https://doi.org/10.1016/j.mtcomm.2026.115829
Received 18 May 2026; Received in revised form 20 July 2026; Accepted 29 July 2026
Available online 29 July 2026

crystalline-to-amorphous and amorphous-to-lithiated phase transitions, combined with the large volume fluctuations, promote crack formation, particle pulverization, electrode delamination, and continuous rupture and reformation of the solid electrolyte interphase (SEI) layer [9]. These degradation mechanisms result in loss of electrical contact, increased irreversible lithium consumption, and rapid capacity fading during cycling [10,11]. Consequently, considerable research efforts have focused on mitigating these structural changes through material engineering strategies such as heteroatomic doping [13,14].

The fabrication of silicon-based composites has shown promise in mitigating the rapid deterioration of silicon anodes [15]. Silicon-based composites usually play a role in buffering direct contact between silicon and the electrolyte, thus reducing the volume expansion problem [16]. Furthermore, adjusting the silicon content in the composition can improve electrical conductivity. For instance, Ulvestad et al. demonstrated that doping silicon with various concentrations of nitrogen (SiN_x: $0.39 \leq x \leq 0.89$), results in improved mechanical stability and an increase in electrical conductivity. However, this results in a decrease in specific capacity from 2345 to 1525 mAh/g over four lithiation cycles for SiN_x, compared to pure silicon, which exhibited a lesser reduction in specific capacity from 2573 to 2107 mAh g^{-1} under the same conditions [17,18]. Wu et al. also demonstrated that doping silicon with carbon can suppress the volume expansion since carbon and silicon form strong covalent bonds that are much harder to break. They also demonstrated that the band gap of the doped structure decreases as the concentration of carbon increases. However, the specific capacity also decreased as the carbon concentration increased, as they reported 3445 and 2977 mAh/g in specific capacity for $Si_{60}C_4$ and $Si_{54}C_{10}$, respectively [19].

Previous studies focusing on the synthesis of silicon-based composites have been done experimentally, such as chemical vapour deposition [20], high-energy mechanical milling [21], and gas-phase methods to synthesize silicon-based composites. For instance, Kim et al. used high-energy mechanical milling (HEMM) to synthesize SiC nanocomposites for 24 h, which exhibited a stable theoretical capacity of ~370 mAh/g. They showed that in this structure, the nanoparticles had diameters of ≅ 10 nm and were evenly distributed [22]. In another instance, Yang et al. built a hollow microsphere of SiC using a template-free synthetic strategy. They combined an in-situ polymerization process to form a precursor and magnesiothermic reduction towards the inner cavity. They found that these hollow microspheres exhibited improved cycling performance (768.7 mAh/g after 100 cycles at 0.84 A/g), and good rate capabilities (497.1 mAh/g at 8.4 A/g) when they used them as an anode material for LIBs. Moreover, the structure maintains structural stability over 100 cycles [23]. Other researchers have also been trying to improve silicon/carbon composites to accommodate the volume expansion from silicon. For example, Ouyang et al. doped porous carbon fibre framework entrapped with silicon nanoparticles with nitrogen using an improved electrospinning strategy [24]. This approach resulted in a Si@NPCNF nanocomposite with high porosity and a large surface area, which effectively alleviated the volume expansion of silicon. Their structure demonstrated outstanding electrochemical performance with initial capacity (1521 mAh/g at 0.1 A/g), good rate capability (648 mAh/g at 2 A/g), and excellent cycle stability (515.5 mAh/g after 200 cycles at 1 A/g). These are only some prominent examples of silicon anode enhancements, leaving room for further exploration of dopants such as carbon, which is known to enhance electrical conductivity and mitigate structural degradation in silicon by strengthening the host lattice [25].

Alongside experimental techniques, advancements in computational materials science and artificial intelligence (AI) are increasingly driving data-informed discovery of energy storage materials [26,27]. Machine learning techniques [26], neural network-based interatomic potentials [28], and high-throughput screening approaches [29] are now being combined with first-principles calculations to speed up the prediction of stable phases, ion diffusion mechanisms, and electrochemical performance in complex materials [27,30,31]. These data-driven approaches significantly reduce the time and computational cost associated with conventional trial-and-error materials discovery while enabling the efficient exploration of vast compositional spaces [32,33]. Among this variety of data-driven computational techniques, the cluster expansion (CE) method has emerged as a powerful statistical framework for modelling configurational disorder in multicomponent crystalline materials [34]. From a machine learning perspective, CE can be regarded as a physics-informed supervised learning approach. By parameterizing effective cluster interactions from density functional theory (DFT) calculations, CE enables rapid and accurate prediction of formation energies across large compositional spaces while retaining first-principles accuracy [35]. To avoid overfitting and efficiently identify the most relevant atomic interactions, the CE method employs sparse-selection techniques such as compressive sensing and genetic algorithms. This iterative process, through which low-energy structures are identified and training datasets are refined, follows an active-learning workflow in which new information is incorporated to improve predictive accuracy. Furthermore, coupling CE with Monte Carlo (MC) simulations extends the length and time scales accessible conventional DFT, enabling reliable investigation of phase stability, order-disorder transitions, and temperature-dependent thermodynamic properties [36]. Consequently, CE complements modern AI-driven materials discovery by providing physically interpretable, computationally efficient, and highly accurate predictions, making it an indispensable tool for the rational design and optimisation of next-generation electrode materials [34,35].

Guided by these computational approaches, doping has emerged as an effective strategy for tailoring the properties of silicon-based anodes. Nitrogen doping has the potential to modify the electronic structure, strengthen chemical bonding, and improve structural stability, thereby mitigating the mechanical degradation associated with repeated volume changes during lithiation and delithiation [37]. Similarly, fluorine, owing to its high electronegativity and strong affinity for silicon, can substantially alter the local bonding environment, electronic structure, and phase stability [38]. Together, these dopants provide diverse and tuneable chemical interactions that offer promising avenues for overcoming the long-standing limitations of silicon as a high-capacity anode material for next-generation lithium-ion batteries.

This work investigates the effect of carbon, fluorine, and nitrogen doping on the structural, electronic and mechanical properties of silicon, aiming to identify silicon-based compounds that can serve as stable and high-performance anode materials for next-generation lithium-ion batteries.

2. Materials and methodology

2.1. Cluster expansion simulation

The Universal Cluster Expansion (UNCLE) code [39] was utilized to generate possible stable and metastable phases of silicon doped with carbon, fluorine, and nitrogen by systematically evaluating a wide range of atomic configurations across the composition space. This was achieved using a genetic algorithm approach, which enables the construction and automatic convergence of a cluster expansion model with partial disorder on one or more sublattices. Three-unit cells were considered during the exploration of the configurational space. The fitting scheme was performed for a maximum of 20 iterations, with up to 10 new structures added per iteration, starting from an initial training set of 10 structures. Model convergence was assessed using the cross-validation score (CVS), where values below 5 meV/atom are considered indicative of high accuracy. The CVS quantifies the predictive performance of the cluster expansion by measuring its agreement with DFT-calculated formation energies [40,41]. The iterative process was considered converged when the CVS fell below the predefined threshold, and no additional low-energy or ground-state structures were predicted in subsequent iterations. Furthermore, the residual errors between the cluster expansion predictions and DFT calculations were

examined and found to be randomly distributed around zero, indicating the absence of systematic bias in the fitted model. Most of the predicted formation energies exhibited only small deviations from the corresponding DFT values, demonstrating the robustness and reliability of the energy predictions. The absence of newly identified ground-state structures, together with the low CVS and well-behaved error distribution, confirmed that the configurational space had been sufficiently sampled and that the cluster expansion model had reached convergence. This approach enables the prediction of formation energies, structural motifs, and thermodynamically favourable arrangements that may not yet have been experimentally identified. A schematic of the self-consistent outer loop that selects input structures for the cluster expansion model is shown in Fig. 1.

2.2. Density functional theory calculation

The density functional theory (DFT) embedded within the Vienna Ab Initio Simulation Package (VASP) code was then used to calculate the structural, mechanical, and electronic properties of the predicted structure [42,43]. The generalized gradient approximation with Perdew-Burke-Ernzerhof (GGA-PBE) [44] correlation functional was used for structural and mechanical properties, whereas for the electronic properties, hybrid functionals with the hybrid type HSE06 were used. All the calculations were carried out with the cut-off energy of 466 eV for SiC, 510 eV for SiN, and 532 eV for SiF_2, SiF_5, SiN_2, and SiN_5. The k-point mesh of 9x9x9 was used for all the structures in the Brillouin zone, which was constructed using the Monkhorst-Pack schemes [45]. The plane-wave energy cutoff and k-point sampling were established through convergence testing and provided sufficient accuracy for reliable structural relaxation of all investigated systems. The phonon dispersion calculations were performed using the PHONON code [46].

3. Results

3.1. Cluster expansion

This section presents the cluster expansion results for $Si_{1-x}M_x$ (M = C, N, and F). The UNCLE code was employed to iteratively optimise each model by refining the effective cluster interactions (ECIs) and predicting new low-energy configurations. Figs. 2(a-f) and 3(a-c) summarize the optimisation process for these compositions. The accuracy of the cluster expansion and the resulting thermodynamic stability trends are revealed by their respective ground-state diagrams.

Fig. 2(a) and (b) illustrate the iterative optimisation process for carbon-doped silicon, showing the progression of the fitting procedure in terms of the number of completed iterations and the number of new structures predicted at the end of each cycle. The cluster expansion converged after eight iterations, during which twenty-five new phases were predicted. As shown in Fig. 2(b), by the eighth iteration, the model achieved a cross-validation score (CVS) of 0.78 meV/position, calculated from the mean-squared error between the predicted energies and the corresponding DFT values [47]. The cross-validation score quantifies the predictive capability of the model for structures not included in the training set, with lower CVS values indicating improved predictive performance and transferability [41,48]. The obtained value is well below the commonly accepted threshold of 5 meV/position [49,50],

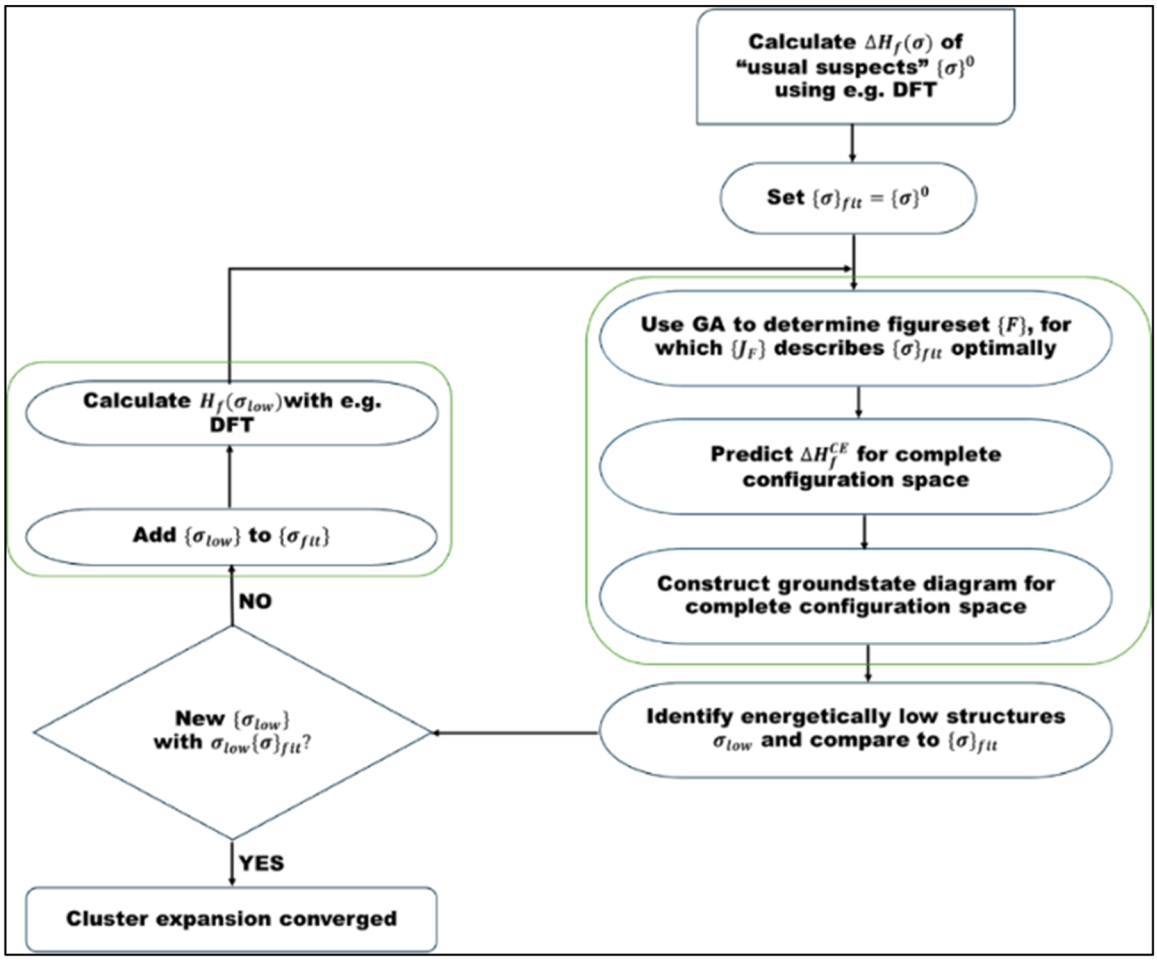

Fig. 1. A visual depiction of the self-consistent outer loop responsible for selecting input structures used in the cluster expansion model [39].

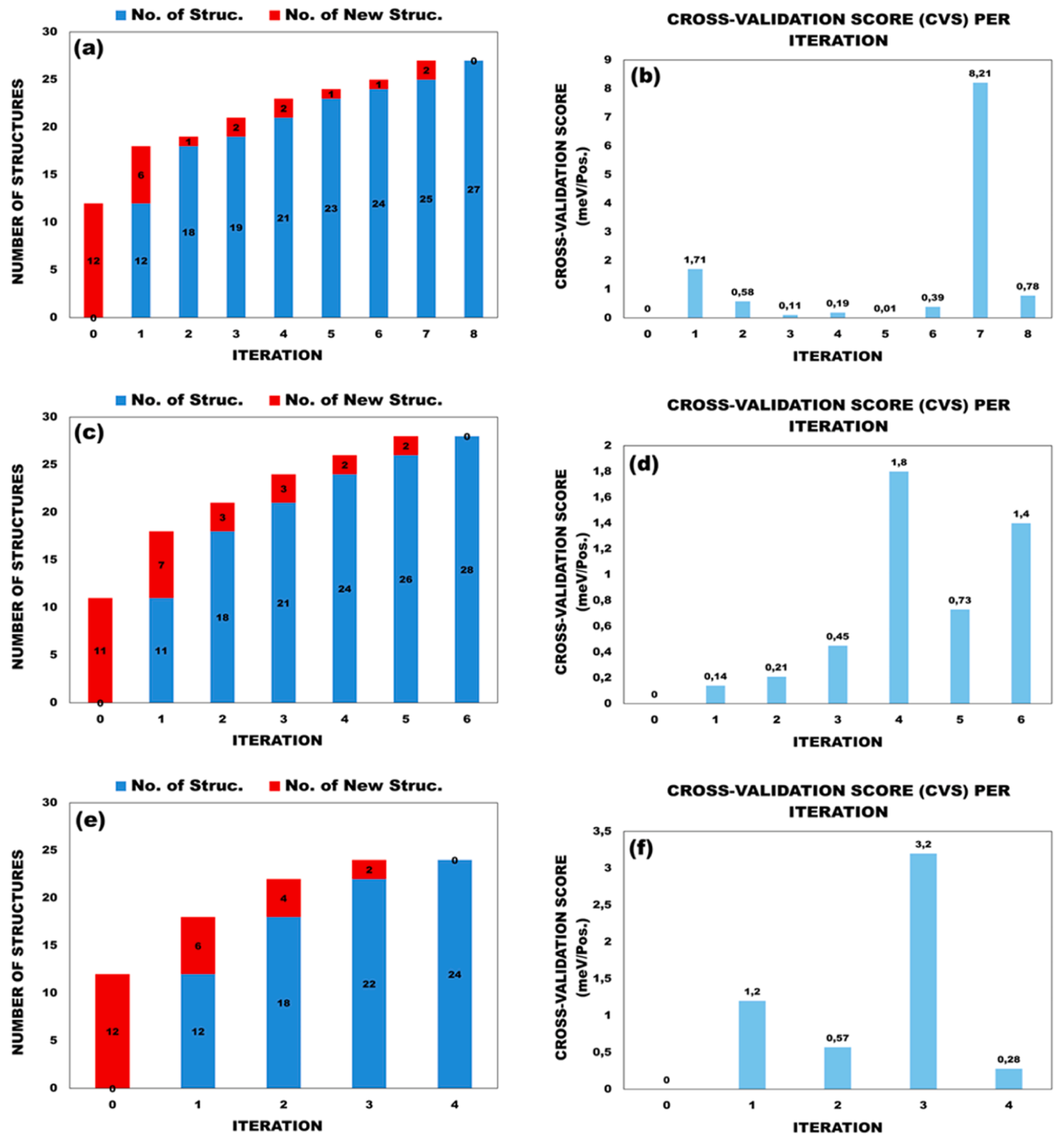

Fig. 2. Graphical representation of the iterative optimisation progress (a, c, e) and the cross-validation score per iteration (b, d, f) for the $Si_{1-x}M_x$ (M=C, N and F) cluster expansion.

which is generally considered sufficient for reliable configuration prediction in alloy and doped-material systems. This low cross-validation score indicates that the effective cluster interactions were accurately captured during the iterative fitting procedure.

For fluorine doping, silicon was alloyed with fluorine at all atomic sites, and the cluster expansion was employed to determine the corresponding ground-state phases. The fitting process converged after six iterations, predicting twenty-six new phases, as illustrated in Fig. 2(c). The convergence behaviour shown in Fig. 2(d) indicates that, by the sixth iteration, the cluster expansion achieved a cross-validation score of 1.40 meV/position. This value remains below the 5 meV/position reliability threshold [49,50], indicating that the model accurately captures the configurational energetics.

Figs. 2(e) and 2(f) present the cluster expansion results for nitrogen-doped silicon. In this case, the fitting procedure required four iterations and yielded twenty-two new predicted phases. As shown in Fig. 2(f), the cross-validation score reached 0.28 meV/position, indicating strong agreement between predicted and DFT-calculated energies and confirming the robustness of the fitted cluster interactions for the nitrogen-doped system.

Fig. 3(a) shows the binary ground-state diagram, summarizing the predicted phases and their formation energies. Green crosses represent cluster expansion formation energies for structures in the training set, while green squares denote the corresponding DFT values. Grey crosses indicate formation energies of all other configurations evaluated by the cluster expansion. Twenty-five new phases are predicted, with most located within the miscibility gap and exhibiting positive heats of formation energies, indicating thermodynamic instability. Only one phase, SiC at 50% Si and 50% C, lies on the DFT ground-state line, identifying it as the only thermodynamically stable compound in the Si-C system.

Fig. 3(b) presents the binary ground-state diagram for fluorine-doped silicon. All predicted structures lie on the miscible constituents' side and display negative heats of formation energies. Of the twenty-six predicted phases, SiF_2 and SiF_5 lie directly on the DFT ground-state line, with formation energies of −3000 and −2400 meV/site, respectively, indicating the lowest energies among the predicted configurations.

Fig. 3(c) shows the ground-state diagram for nitrogen-doped silicon. All predicted structures appear on the miscible side with negative heats of formation. Among the twenty-two predicted phases, SiN, SiN_2, and SiN_5 lie on the DFT ground-state line, with formation energies of −2400, −2250, and −1700 meV/site, respectively. Comparison of these values shows that phases with higher nitrogen content exhibit less negative formation energies than SiN.

3.2. Structural properties

This subsection presents a structural analysis of the pristine silicon and doped silicon phases obtained from cluster expansion simulations. The analysis focuses on the optimised lattice parameters, space-group symmetries, Wyckoff positions, and interatomic bond lengths of the generated structures. These crystallographic descriptors are examined to characterize unit-cell dimensions, atomic arrangements, and local bonding environments across the carbon, fluorine, and nitrogen-doped systems. Where available, the calculated structural parameters are compared with experimental reference data to document and validate the crystallographic features of the predicted phases.

The lattice parameters of silicon and carbon structures are in good agreement with the experimental values, having a percentage difference of 0.1% (Table 1). Both structures are cubic in crystal symmetry, with the optimised SiC structure adopting the F-43m space group. This structure was identified as the most thermodynamically stable phase among those generated during cluster expansion simulation, as indicated by its lowest heat of formation. Fig. 4(a) shows the unit cell of the SiC, where silicon atoms occupy the Wyckoff positions at (0, 0, 0), and carbon atoms are located at ($\frac{1}{4}$, $\frac{1}{4}$, $\frac{1}{4}$). The atoms are tetrahedrally coordinated.

The cluster expansion predicted two most thermodynamically stable phases, SiF_2 and SiF_5. Upon symmetry refinement and geometry optimisation, both structures adopted an orthorhombic crystal symmetry ($a \neq b \neq c$ and $\alpha = \beta = \gamma = 90^0$), which could be beneficial to volume expansion associated with silicon lithiation. Moreover, orthorhombic structures tend to exhibit lower atomic packing density as compared to cubic systems. The unit cells of these structures, as shown in Fig. 4(b and

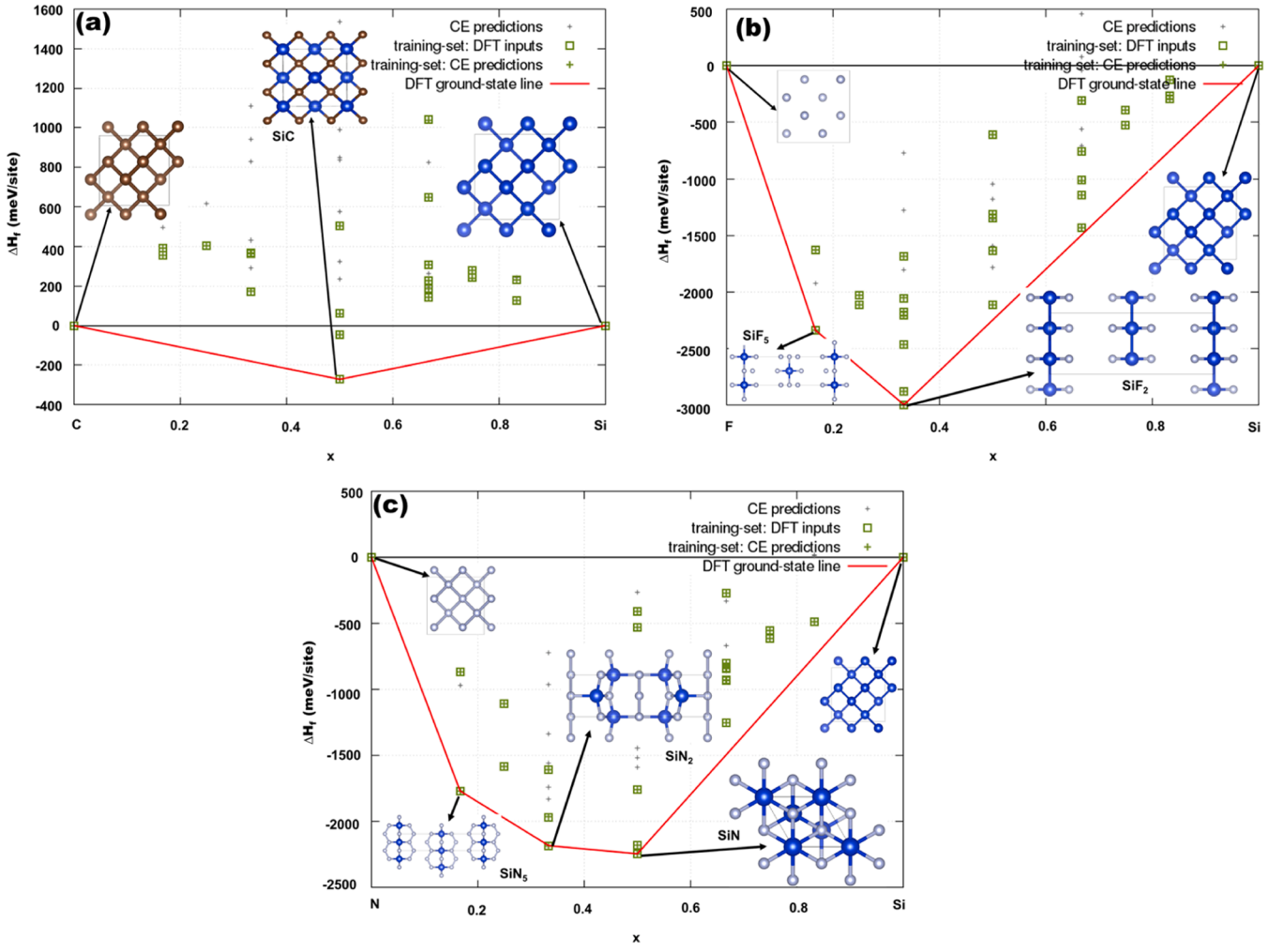

Fig. 3. Binary ground state diagram of $Si_{1-x}M_x$ (M = C, N, and F) and the structure lying on the DFT ground-state line.

Table 1
Lattice parameters of the predicted structures from Si1-xMx (M=C, F and N) cluster expansion.

Structure	Space group	Lattice parameter (Å)			Angle (°)	
		a	b	c	α	Γ
Si	Fd-3m	5.47 (5.48 [51])			90.0	
C	Fd-3m	3.57 (3.57 [52])			90.0	
N	Fd-3m	4.19			90.0	
F	Fd-3m	4.84			90.0	
$Si_{1-x}C_x$						
SiC	F-43m	4.38 (4.38 [53])			90.0	
$Si_{1-x}F_x$						
SiF_2	Imma	11.00	4.11	5.39	90.0	
SiF_5	Imm2	10.69	3.34	5.42	90.0	
$Si_{1-x}N_x$						
SiN	R-3m	2.91		21.60	90.0	120.0
SiN_2	Imm2	9.25	2.83	4.84	90.0	
SiN_5	Imm2	11.41	2.33	5.30	90.0	

c), show that silicon atoms occupy 2a Wyckoff positions, while fluorine atoms are located at 2b and 4c Wyckoff positions. Lattice parameters of SiF_2 and SiF_5 indicate that the structures are more compact, which shows structural stability.

For nitrogen-doped silicon, the crystal structures of SiN, SiN_2 and SiN_5 are also shown in Fig. 4(d-f), with their structural parameters summarised in Table 1. SiN exhibited a hexagonal symmetry, with silicon atoms occupying high-symmetry Wyckoff positions and nitrogen occupying lower-symmetry positions. This arrangement suggests that the structure is layered and shows anisotropic bonding with strong in-plane and weaker interlayer interactions. The lattice parameters suggest a compact layered arrangement in on two crystallographic directions and elongation along the third, which suggests structural stability. SiN_2 and SiN_5 both adopted an orthorhombic symmetry and have the same space group. The SiN_5 is layered in a way that the nitrogen atoms form trigonal symmetry with the silicon atoms. All three structures exhibit strong covalent bonding.

Table 2 presents the calculated bond lengths for pristine elements and the doped silicon structures. The Si-Si bond length in pure silicon is calculated to be 2.36 Å, which closely matches the experimental value of 2.37 Å [51], indicating good agreement between the computational results and reported data. Similarly, the C-C bond length of 1.55 Å is consistent with the experimental value of 1.55 Å [52]. In the $Si_{1-x}C_x$ system, the SiC phase exhibits a Si-C bond length of 1.96 Å, which is slightly larger than the reported experimental value of 1.88 Å [53]. This bond length reflects strong covalent interactions between silicon and carbon atoms within the tetrahedrally coordinated structure.

For the fluorine-doped silicon phases, both SiF_2 and SiF_5 display Si-F bond lengths of approximately 1.93 Å. The SiF_2 structure also contains Si–Si bonds with a length of 2.60 Å, which is longer than the Si-Si bond length in pure silicon, suggesting a modification of the local bonding environment upon fluorine incorporation. In the nitrogen-doped structures, SiN exhibits Si-N bonds of 2.12 Å together with Si-Si bonds of 2.60 Å. The SiN_2 and SiN_5 phases contain N-N bonds of 1.88 Å and Si-N bonds of 2.12 Å, while SiN_5 additionally includes Si-Si bonds of 2.60 Å. These variations in bond lengths illustrate the changes in local atomic arrangements introduced by different dopant species, reflecting the distinct bonding environments present in the predicted silicon-based compounds.

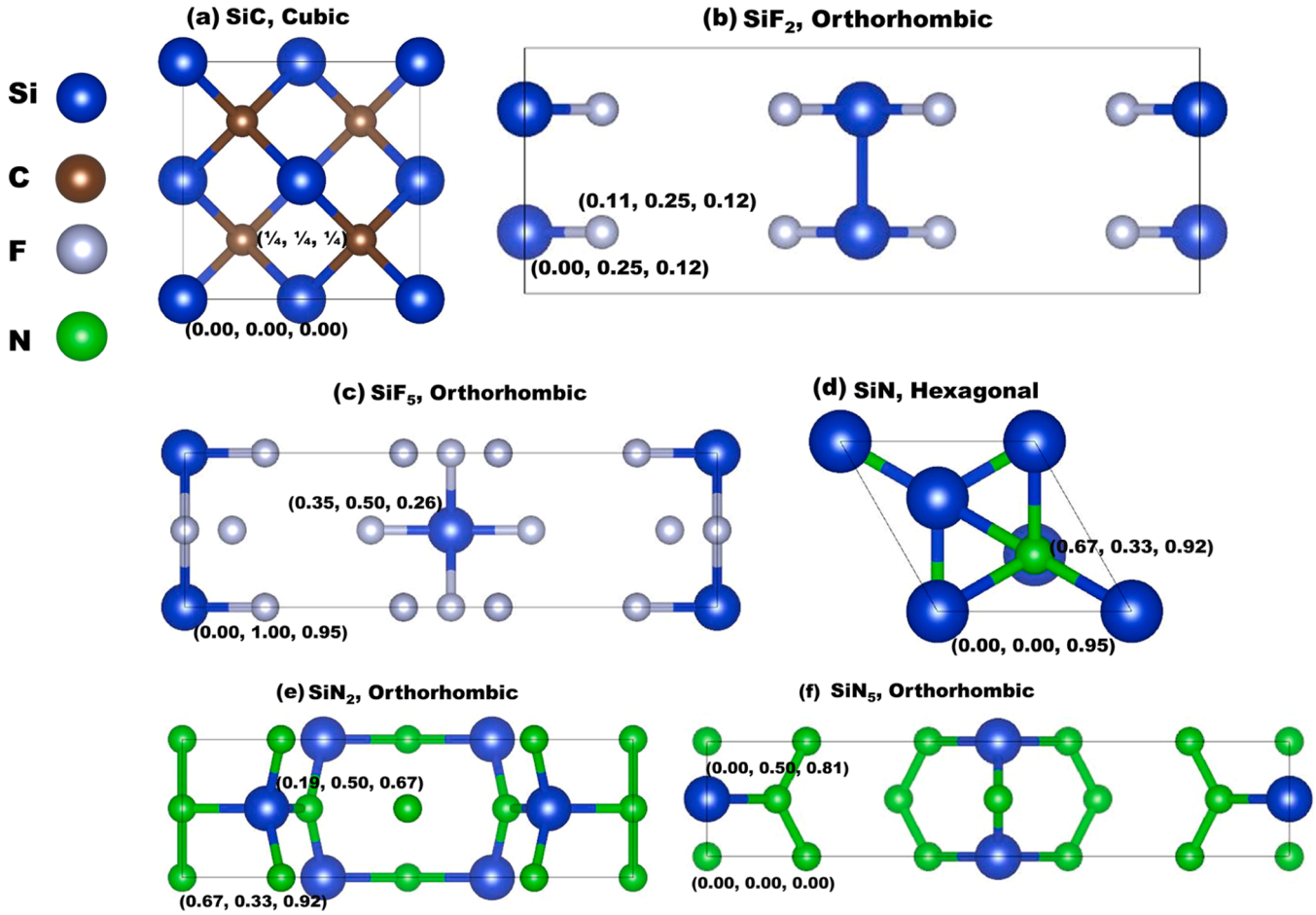

Fig. 4. Schematic crystal structures of $Si_{1-x}M_x$ (M = C, F and N) as predicted by cluster expansion.

Table 2
Bond lengths of the predicted structures from $Si_{1-x}M_x$ (M=C, F and N) cluster expansion.

Structure	Bond length (Å)	
Si	Si-Si	2.36 (2.37 [51])
C	C-C	1.55 (1.55 [52])
N	N-N	1.81
F	F-F	-
$Si_{1-x}C_x$		
SiC	Si-C	1.96 (1.88 [53])
$Si_{1-x}F_x$		
SiF_2	Si-F	1.93
	Si-Si	2.60
SiF_5	Si-F	1.93
$Si_{1-x}N_x$		
SiN	Si-N	2.12
	Si-Si	2.60
SiN_2	N-N	1.88
	Si-N	2.12
SiN_5	N-N	1.88
	Si-N	2.12
	Si-Si	2.60

3.3. Electronic properties of pure Si and Si1-xMx (M= C, N, F)

Understanding the electronic behaviour of silicon and its doped derivatives is essential for evaluating their suitability in energy storage applications, particularly in systems where charge transport, conductivity, and structural stability are critical. To this end, the electronic arrangement of silicon and the most stable doped phases was examined through density functional theory (DFT) calculations, focusing on the total and partial density of states (TDOS and PDOS) as well as the electronic band structures. The TDOS provides insight into the overall distribution of electronic states and the presence or absence of a band gap, while the PDOS reveals the orbital-specific contributions responsible for bonding and electronic activity. Complementing these, the band structure clarifies whether the material exhibits direct or indirect band gaps and highlights features, such as band dispersion and the positions of the valence band maxima and conduction band minima that influence charge carrier mobility. Together, these analyses establish a detailed picture of how doping with carbon, nitrogen, and fluorine modifies the intrinsic semiconducting behaviour of silicon, enabling a comparison of how each dopant affects band gap width, orbital participation, metallic or semiconducting character, and structural stability.

The electronic structure of silicon was examined to determine its electronic configuration. Fig. 5(a) shows the TDOS for silicon, highlighting that it is a semiconductor with an indirect band gap of 1.27 eV, which is in good agreement with the theoretical value of 1.17 eV [51] (within an error margin of 8%). The partial density of states (PDOS) reveals how each orbital contributes to the overall electronic structure of the material. It is observed from the PDOS that a major contribution to the TDOS emanates from the p-orbital (red). The band structure of silicon, also shown in Fig. 5(b), exhibits an indirect band gap of 1.27 eV. There is no overlap of bands between the valence and conduction bands, further confirming the semiconducting nature observed in the DOS. Furthermore, it is observed that the maxima in the valence band are located at the gamma position, whereas the minima in the conduction band are located near the x-position.

The density of states for SiC depicted in Fig. 6(a) below shows an indirect band gap of 2.31 eV, which suggests that the material is a semiconductor. The calculated band gap compares well with the theoretical one (2.30 eV [54]), with the percentage difference being 0.43%. Carbon doping on silicon increased the band gap from 1.27 eV to 2.31 eV. The wider band gap of SiC could be beneficial in the design of high voltage and power LIBs, with low power loss and favourable properties such as high breakdown voltage, low current leakage and fast switching speed. The PDOS shows that a major contribution to the SiC structure comes from the p-orbital of the carbon atoms, indicated by their high peak intensity. The low peak intensity along the Fermi suggests structural stability of the SiC structure. The band structure of SiC (Fig. 6(b)) is similar to that of silicon, with the maxima and minima located in the Brillouin zone direction. However, for this band structure, the band gap is wider than that shown on carbon, as already observed from the DOS, which is 2.31 eV. This further validates the semiconducting nature of SiC, as no overlapping bands between the conduction and valence bands can be observed.

The increase in the band gap from 1.27 eV for pure silicon to 2.31 eV for SiC can be attributed to strong hybridization between the Si 3p and C 2p orbitals. The shorter Si-C bond lengths promote greater orbital overlap, resulting in stronger covalent bonding and enhanced bonding-

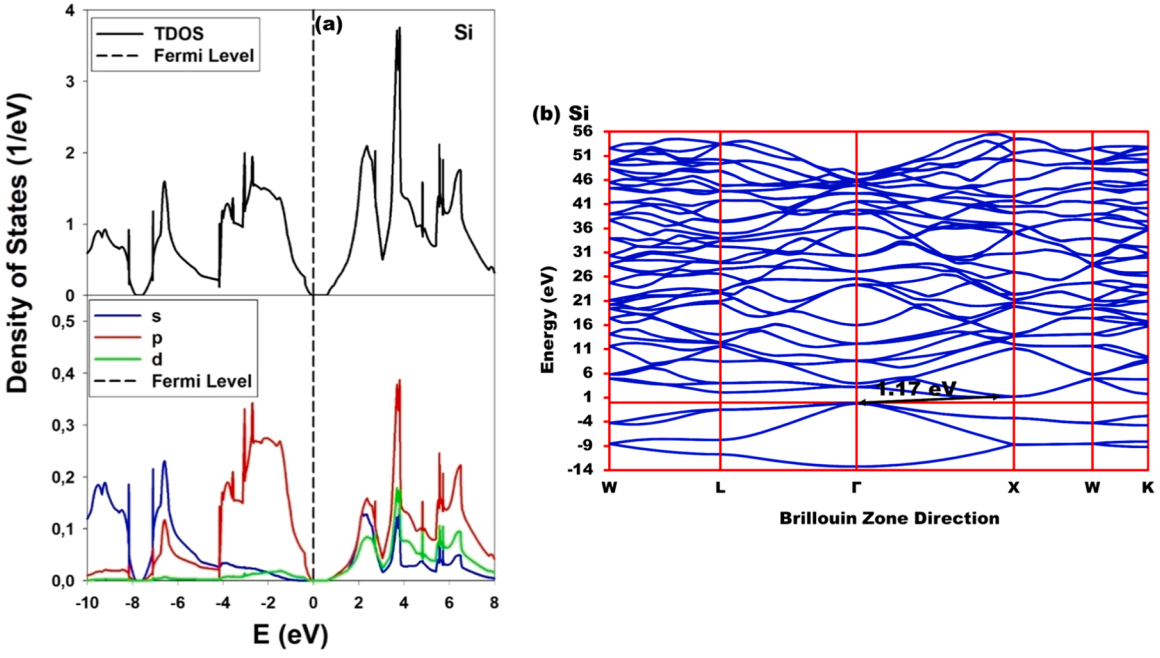

Fig. 5. (a)The total density and partial density of states along with (b) the band structure of Si.

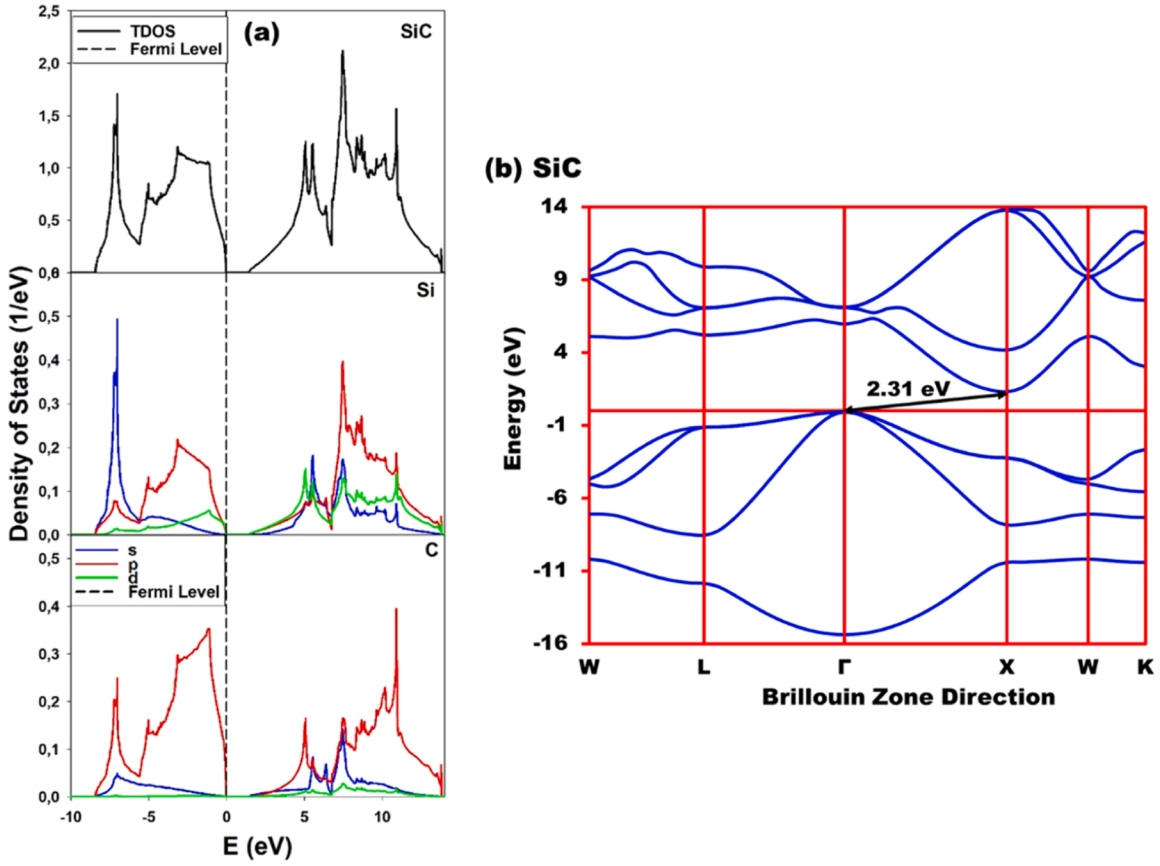

Fig. 6. (a) The total density and partial density of states along with (b) band structure of SiC.

antibonding splitting. This increased splitting widens the energy separation between the valence and conduction bands, leading to a larger band gap and stronger semiconducting behaviour. The PDOS further supports this observation, with the C 2p orbitals contributing significantly to the electronic states near the valence band, indicating that carbon plays a dominant role in modifying the electronic structure. Consequently, carbon doping enhances electron localization and stabilizes the bonding states, resulting in the observed bandgap broadening and improved electronic stability of the SiC phase.

Figs. 7 and 8 illustrate the electronic behaviour of SiF_2 and SiF_5, respectively. The DOS for SiF_2 (Fig. 7a) exhibits a direct band gap of 2.08 eV, consistent with its semiconducting nature. The band structure (Fig. 8a) also shows the semiconductor with a direct band gap, with the maxima in the valence band and minima in the conduction band along the s-position in the Brillouin zone direction. Furthermore, there are no overlapping bands between the conduction and valence bands. The PDOS reveals that the p-orbitals of fluorine atoms contribute most significantly, as reflected by the higher peak intensities. In contrast, the electronic structure of SiF_5 (Fig. 7b) reveals semi-metallic behaviour due to the absence of a visible band gap at the Fermi level. This suggests that electrons can readily transition between the valence and conduction bands. Furthermore, the band structure of SiF_5 (Fig. 8b) shows overlapping bands between the valence and conduction bands, which further validates its semi-metallic behaviour. Whereas the PDOS shows that in SiF_2 and SiF_5, the major contributions arise from the fluorine 2p-orbitals, which exhibit more intense peaks. Comparative analysis of the two structures indicates that SiF_2 is more structurally stable than SiF_5, as evidenced by its lower peak intensity at the Fermi level. The transition from semiconducting SiF_2 to semi-metallic SiF_5 arises from increased Si 3p-F 2p orbital hybridization at higher fluorine concentrations, which broadens the electronic bands, introduces partially occupied states at the Fermi level, and ultimately causes band overlap and metallization.

Fig. 9(a) shows the DOS for SiN, which exhibits an indirect band gap of 1.76 eV. The corresponding band structure in Fig. 10(a) shows no overlap between the valence and conduction bands. The PDOS indicates that the nitrogen p-orbitals provide the dominant contribution, as reflected by the highest peak intensities. Figs. 9b and 9(c) display the DOS of SiN_2 and SiN_5, respectively. In both structures, no band gap is observed. The PDOS analysis shows that the dominant contribution arises from the nitrogen 2p orbitals. Figs. 10b and 10(c) show overlap between the valence and conduction bands, with the Fermi level intersecting these bands. The DOS profiles of SiN_2 and SiN_5 show a continuous distribution of states around the Fermi level. Comparison of the DOS at the Fermi level indicates low intensity for all three structures. Among the three phases, SiN shows the lowest DOS intensity at the Fermi level. The transition from semiconducting SiN to semi-metallic SiN_2 and SiN_5 arises from enhanced hybridization between Si 3p and N 2p orbitals at higher nitrogen concentrations, which broadens the electronic bands, reduces the bonding-antibonding energy separation, and ultimately causes band overlap at the Fermi level, leading to metallization.

3.4. *Mechanical properties*

In this section, the mechanical properties of silicon and its doped derivatives are evaluated to assess their structural integrity and suitability for applications where materials must withstand stress, deformation, and repeated cycling, such as in lithium-ion batteries. Elastic constants provide the fundamental description of how a crystal responds to applied stress, with each crystal symmetry defined by a specific number of independent elastic constants that form its stiffness matrix. These constants, together with derived moduli such as the bulk, shear, and Young's moduli, allow for the assessment of rigidity, compressibility, and resistance to shear deformation.

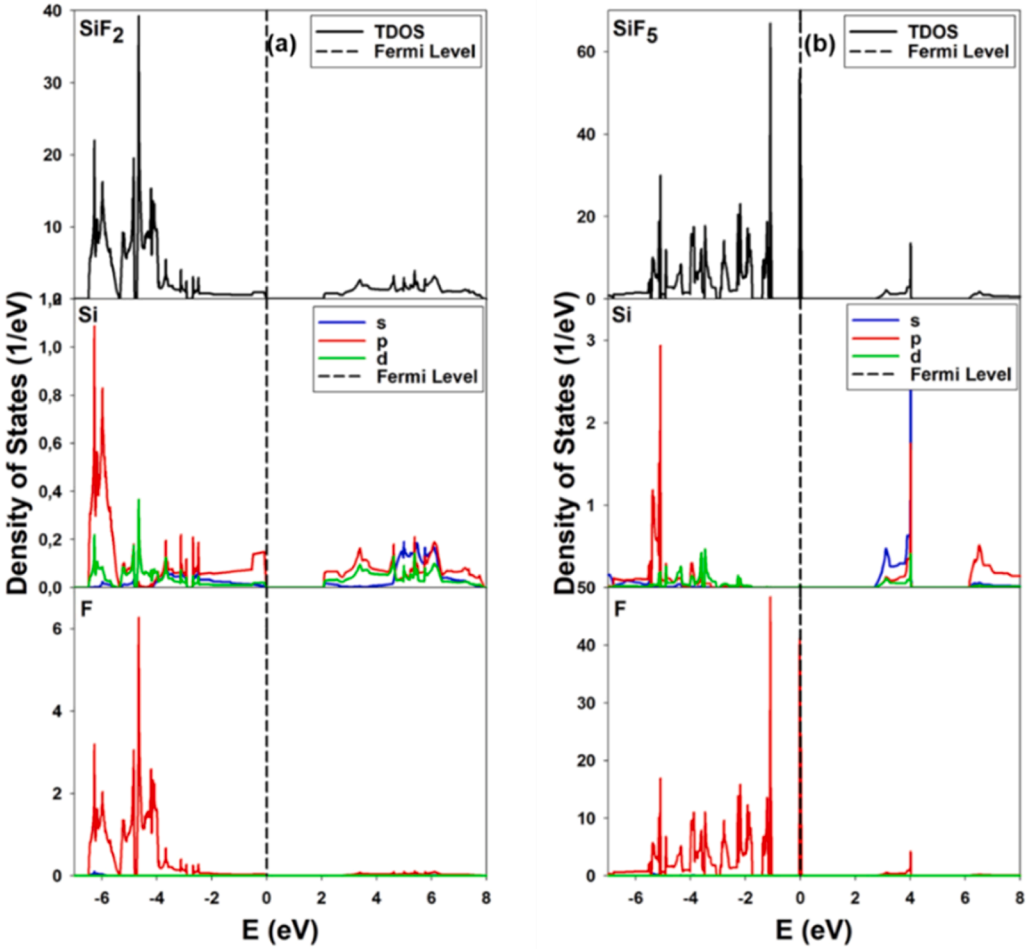

Fig. 7. The total density and partial density of states of (a) SiF_2 and (b) SiF_5.

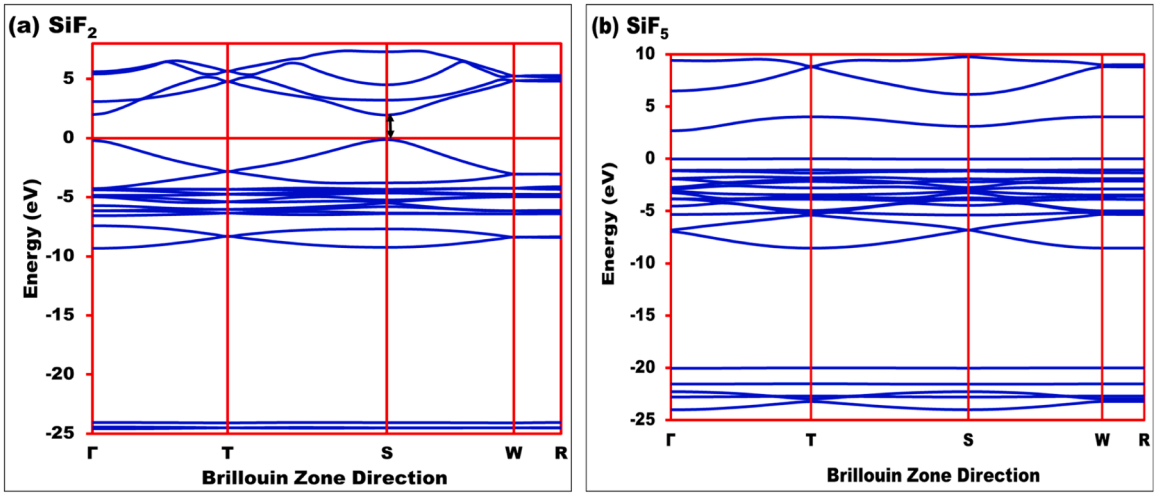

Fig. 8. Electronic band structure of (a) SiF_2 and (b) SiF_5.

Mechanical stability is further examined using the Born stability criteria, which define the conditions under which a crystal maintains positive strain energy under deformation. Complementary descriptors such as Pugh's ratio (B/G) and Poisson's ratio (ν) help classify materials as ductile or brittle, providing critical information for predicting fracture susceptibility during lithiation-induced volume changes.

The mechanical behaviour of cubic, hexagonal, and orthorhombic structures is analysed to determine how carbon, nitrogen, and fluorine doping influence the stiffness, stability, and ductility of silicon-based phases. By comparing their elastic constants and moduli against the corresponding symmetry specific Born criteria, the discussion highlights which structures remain mechanically robust and which exhibit inherent instabilities that may limit their practical applicability.

Elastic constants describe the material's response to stress and strain

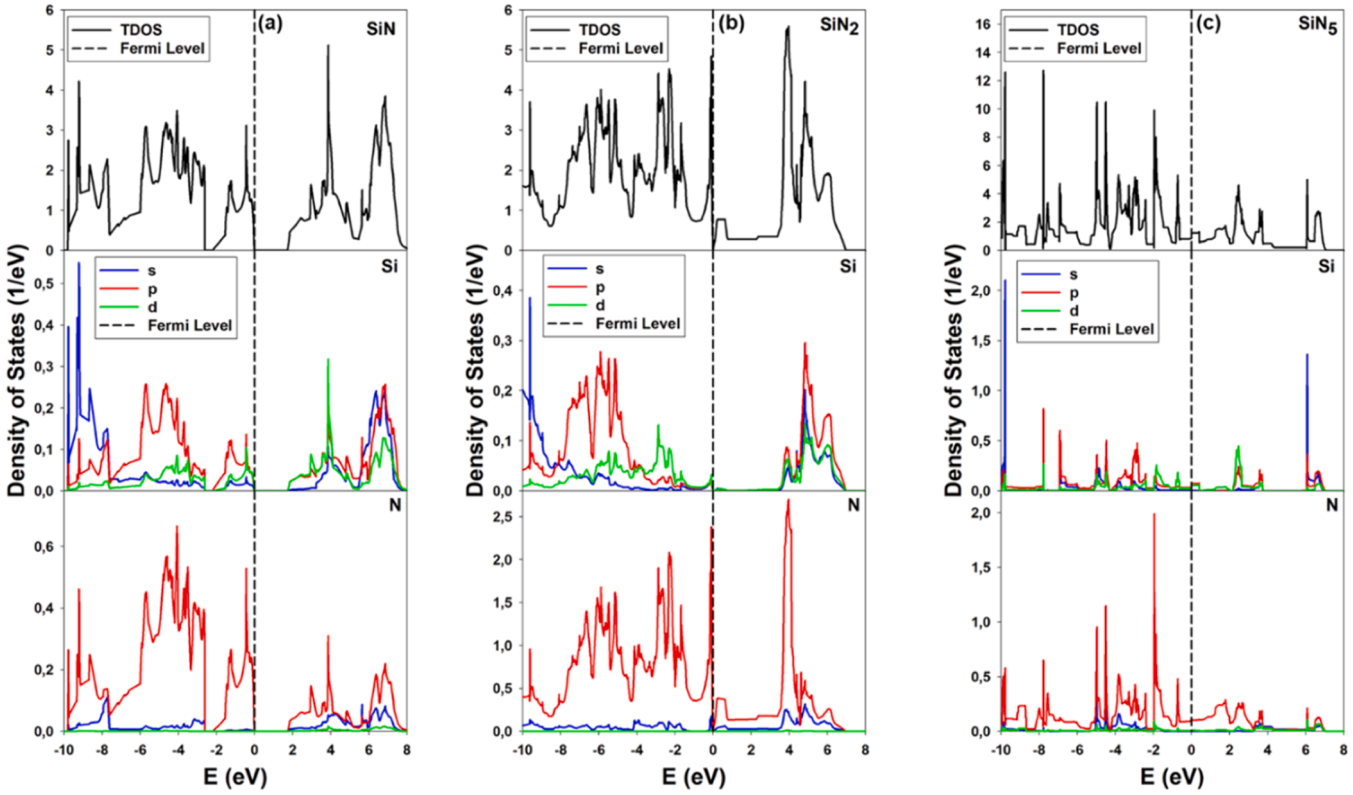

Fig. 9. The total density and partial density of states of (a) SiN, (b) SiN_2 and (c)SiN_5.

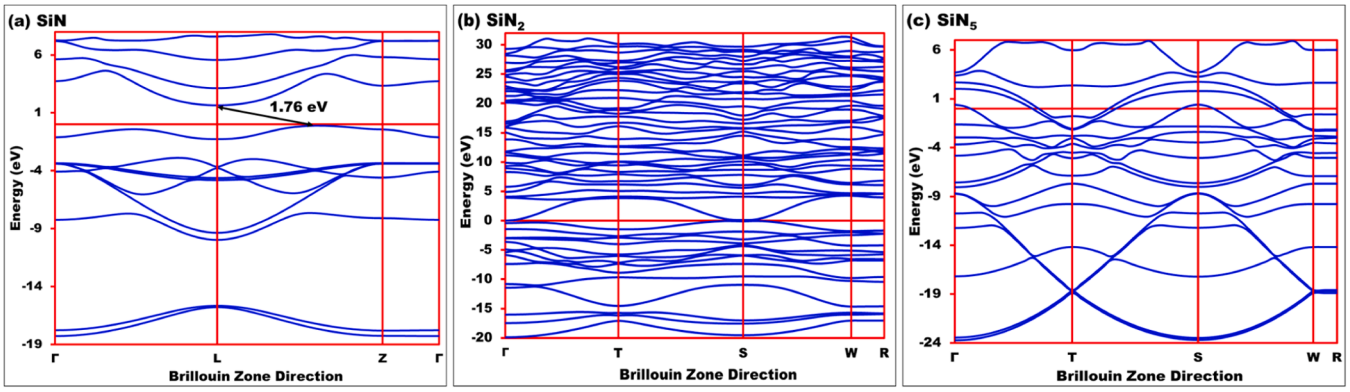

Fig. 10. Electronic band structure of (a) SiN, (b) SiN_2 and (c) SiN_5.

along different crystallographic directions, considering the symmetry of the cubic crystal structure. When expressing the elastic constants in terms of a cubic crystal's stiffness matrix, we refer to three independent elastic constants C_{ij} (C_{11}, C_{12}, C_{44}) for a cubic system the Born stability criterion [55] is shown in Appendix A. Table 3 lists the calculated elastic constants for silicon and SiC.

Silicon and SiC are both mechanically stable as they satisfy the Born stability criterion for cubic structures. The elastic constants of SiC are much higher than those of silicon, which indicates that it is more mechanically stable than silicon. The elastic anisotropy of silicon and silicon carbide was evaluated using the Zener anisotropy factor [56]. Silicon exhibits moderate anisotropy (A = 1.46), whereas SiC displays a higher degree of anisotropy (A = 1.87). The increased anisotropy of SiC originates from the strong directional covalent bonding between Si and C atoms, which enhances stiffness but may also promote localized stress concentrations.

Table 3
Elastic constants for cubic structure and the anisotropy value.

Properties	Si	SiC
C_{11}	150.02	378.69
C_{12}	59.17	127.65
C_{44}	66.23	235.32
A_1	1.46	1.87

Table 4 lists the elastic constants for the SiN hexagonal structure. The crystal has five independent elastic constants (C_{11}, C_{12}, C_{13}, C_{33}, and C_{44}), which define the stiffness matrix. According to the Born stability criterion [55] in Appendix A, the structure satisfies all stability requirements, confirming that it is mechanically stable. However, SiN is highly elastically anisotropic material, as shown by $A_1 = 0.31$ and $A_2 = 0.23$. This indicates strong directional dependence of its elastic response, likely arising from anisotropic Si-N bonding in the hexagonal lattice. While the structure remains stable under stress, its anisotropy

Table 4
Elastic constants for hexagonal structures and the directional anisotropy indices A_1 and A_2.

Properties	SiN
C_{11}	410.30
C_{12}	106.49
C_{13}	20.61
C_{33}	20.91
C_{44}	47.22
A_1	0.31
A_2	0.23

may lead to non-uniform strain distribution during lithiation, which is an important consideration for battery-anode performance.

Si_2F_4, SiF_5, SiN_2 and SiN_5 have an orthorhombic symmetry. Therefore, their mechanical stability is evaluated using nine independent elastic constants: C_{11}, C_{12}, C_{13}, C_{22}, C_{23}, C_{33}, C_{44}, C_{55}, and C_{66}. These constants define the crystal's stiffness matrix for an orthorhombic system, along with the Born stability criterion [55] shown in Appendix A.

The SiN_2 structure meets all the conditions of the Born stability criterion for an orthorhombic crystal structure, indicating its mechanical stability. This structure is well-suited to maintain its shape, integrity, and performance when subjected to external forces, stress or deformation, implying that it can maintain its structural stability under various conditions. In contrast, SiF_2, SiF_5, and SiN_5 fail to satisfy the Born stability criteria for orthorhombic symmetry, since they have a negative C_{ii}. This negative C_{ii} implies that this material would release energy when it is compressed or stretched along this axis, violating the principle of positive strain energy [57]. Hence, these structures are mechanically unstable and are unlikely to maintain their shape or to resist external forces, This compromises the safety and performance of these materials.

The anisotropy factors (A_1, A_2, A_3) of SiF_2, SiF_5, SiN_2, and SiN_5 reveal a strong dependence of elastic behaviour on crystallographic direction, highlighting pronounced differences between fluorine- and nitrogen-doped silicon systems. In SiF_2, the relatively high values of $A_1 = 2.38$, $A_2 = 1.16$, and $A_3 = 1.36$ indicate significant elastic anisotropy, particularly in shear deformation modes, suggesting that the material exhibits strong directional stiffness and uneven stress distribution under mechanical loading. SiF_5 also displays marked anisotropy, with $A_1 = 1.36$, $A_2 = 1.43$, and a higher $A_3 = 2.09$, indicating that its mechanical response is highly direction-dependent, especially along one crystallographic orientation, which is consistent with the distorted bonding environment induced by higher fluorine incorporation. In the case of SiN_2, the anisotropy remains pronounced with $A_1 = 2.31$ and $A_3 = 2.27$, while $A_2 = 0.96$ is close to unity, indicating near-isotropic behaviour in one deformation mode. This suggests that although SiN_2 is elastically anisotropic, it retains a more balanced mechanical response compared to the fluorinated phases and can accommodate directional strain more effectively, consistent with its predicted mechanical stability and ductility. In contrast, SiN_5 exhibits negative anisotropy values ($A_1 = -0.32$, $A_2 = -0.20$, $A_3 = -0.11$), which signifies a breakdown of mechanical stability and indicates that the structure would not sustain positive elastic resistance under deformation.

The calculated elastic moduli, along with Pugh and Poisson's ratio, are plotted in Fig. 11 to determine whether the predicted structures will be able to withstand external forces and stress from all different directions.

The shear, bulk, and Young's moduli of SiC are higher than those of pure silicon, indicating greater resistance to applied stress and strain. The ductility or brittleness of these materials can be assessed using Pugh's ratio (B/G) [58]. Materials with B/G values greater than 1.75 generally indicate ductility, whereas those with values below 1.75 signify brittleness. SiC exhibits a Pugh's ratio of 1.16, classifying it as brittle and therefore susceptible to deformation and fracture. This behaviour is further supported by its Poisson's ratio [59], which is significantly lower than the recommended ductile threshold of 0.26.

Table 5
Elastic constants for orthorhombic structures and the anisotropic indices A_1, A_2 and A_3.

Properties	SiF_2	SiF_5	SiN_2	SiN_5
C_{11}	15.56	9.41	218.81	26.10
C_{12}	−4.56	−8.05	47.83	−0.10
C_{13}	−3.82	5.28	105.60	15.15
C_{22}	67.00	90.58	471.88	618.32
C_{23}	13.31	−4.48	88.65	3.96
C_{33}	21.90	12.54	297.46	30.35
C_{44}	23.94	11.90	197.39	−4.13
C_{55}	−3.28	−3.71	4.61	26.91
C_{66}	11.48	−52.06	86.86	37.29
A_1	2.38	1.36	2.31	−0.32
A_2	1.16	1.43	0.96	−0.20
A_3	1.36	2.09	2.27	−0.11

Although carbon doping enhances the elastic constants (Cij) and moduli relative to pure silicon, it reduces both Pugh's and Poisson's ratios, indicating that SiC is more brittle than silicon.

Similarly, the Poisson's and Pugh's ratios of SiN fall below the critical values of 0.26 and 1.75, respectively, suggesting brittle mechanical behaviour and a tendency toward fracture under external loading. In contrast, SiN_2 exhibits a Pugh's ratio greater than 1.75 and a Poisson's ratio exceeding 0.26, indicating ductile behaviour and enhanced resistance to deformation. This ductility suggests that SiN_2 may accommodate lateral strain during lithiation and better tolerate volume changes during electrochemical cycling. Conversely, SiF_2, SiF_5, and SiN_5 display Pugh's ratios below 1.75 and Poisson's ratios less than 0.26, classifying them as brittle materials that are more prone to deformation and cracking when subjected to external forces.

4. Phonon dispersion curves

In this section, the phonon dispersion curves of silicon and its derivatives, SiC and SiN, were found to be vibrationally stable, as evidenced by the absence of imaginary frequencies throughout the Brillouin zone and the presence of only positive phonon modes [53]. This indicates that these structures correspond to local minima on the potential energy surface and are therefore dynamically stable against small lattice perturbations. The stability of SiC and SiN can be attributed to the strong covalent bonding arising from the hybridization of Si 3p orbitals with C 2p and N 2p orbitals, respectively. Such strong orbital overlap enhances the interatomic force constants and results in stable lattice vibrations across all wave vectors.

In contrast, SiF_2, SiF_5, SiN_2, and SiN_5 exhibit imaginary phonon frequencies, indicating dynamical instability. The instability becomes more pronounced with increasing dopant concentration, particularly for SiN_2 and SiN_5, which display significant negative phonon branches along several high-symmetry directions. The presence of these soft modes suggests a tendency for the crystal lattice to undergo structural distortion or transformation to a lower-energy configuration. This behaviour may be attributed to changes in orbital hybridization and bonding characteristics caused by the higher concentration of dopant atoms, which alter the electronic structure and weaken the restoring forces responsible for maintaining lattice stability. Consequently, while some of these phases may satisfy thermodynamic or mechanical stability criteria, their phonon spectra indicate that they are dynamically unstable at 0 K.

This dynamical stability is a critical requirement for maintaining structural integrity during repeated lithiation and delithiation cycles. Dynamically stable phases such as SiC and SiN are expected to better withstand the stresses induced by lithium insertion and extraction, thereby reducing the likelihood of crack formation, particle pulverization, and electrode degradation. Furthermore, a stable crystal lattice promotes the formation of a more robust solid electrolyte interphase (SEI) layer, which is essential for long-term cycling performance.

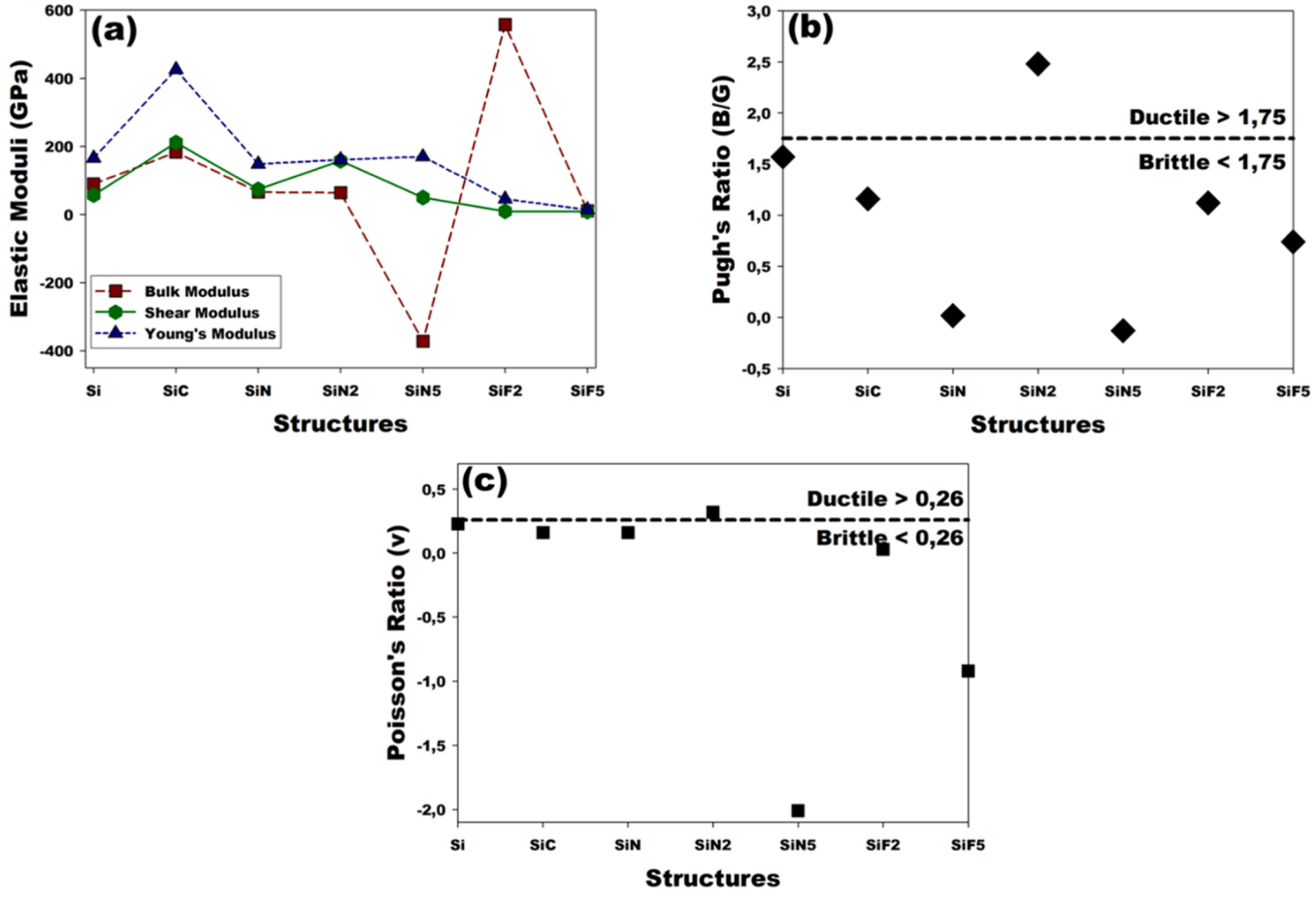

Fig. 11. (a) Elastic moduli (Bulk (B), Shear (G), Young's (E) moduli), (b) Pugh's (B/G) and (c) Poisson's (v) ratio.

Conversely, the dynamically unstable phases may undergo structural transformations during electrochemical cycling, leading to accelerated capacity fading, loss of electrical contact, and reduced cycle life.

5. Discussion

The cluster expansion results for $Si_{1-x}M_x$ (M = C, N, and F) revealed significant differences in the thermodynamic, structural, and electronic stability of the doped systems, underscoring the profound influence of dopant type on silicon's intrinsic properties. The iterative optimisation process using the Universal Cluster Expansion (UNCLE) code demonstrated high predictive accuracy across all systems, with cross-validation scores that are well below the 5 meV/position threshold, confirming the reliability of the predicted low-energy configurations [49,50]. The ground-state diagrams showed distinct stability patterns depending on the dopant, while carbon-doped silicon generated mostly unstable structures with positive heats of formation; fluorine- and nitrogen-doped systems produced several thermodynamically stable compounds with negative formation energies.

The combined thermodynamic, electronic, mechanical, and vibrational analyses reveal distinct effects of carbon, fluorine, and nitrogen doping on the properties of silicon. For the carbon-doped system, only one ordered phase, SiC, was located on the DFT ground-state line, confirming its thermodynamic stability. The cubic F-43m structure, together with shorter Si-C bond lengths compared to Si-Si bonds in pure silicon, indicates stronger covalent interactions arising from significant hybridization between Si 3p and C 2p orbitals. This enhanced bonding increases structural rigidity and contributes to the widening of the band gap from 1.27 eV for silicon to 2.31 eV for SiC. Phonon calculations further confirmed the dynamical stability of SiC through the absence of imaginary frequencies across the Brillouin zone. Although the strong covalent bonding improves thermal and structural stability, the low Pugh's ratio (1.16), Poisson's ratio (0.16) and moderate anisotropy (A = 1.87) suggest brittle, direction-dependent behaviour that may promote stress concentration during cycling, suggesting that SiC may be susceptible to fracture under the repeated volume changes associated with lithiation and delithiation.

Fluorine doping produced two thermodynamically stable phases, SiF_2 and SiF_5, both exhibiting negative formation energies and orthorhombic crystal symmetry. Electronic structure calculations showed that SiF_2 is a semiconductor with a direct band gap of 2.08 eV, while SiF_5 exhibits semi-metallic behaviour due to the overlap of valence and conduction bands at the Fermi level. This transition from semiconducting to semi-metallic behaviour can be attributed to the increased contribution of F 2p states near the Fermi level, which modifies the Si-F hybridized electronic states and promotes electronic delocalization. Despite these favourable electronic characteristics, both fluorine-containing phases were found to be mechanically unstable, failing to satisfy the Born stability criteria [55]. The phonon dispersion curves further reveal the presence of imaginary frequencies, confirming dynamical instability in these fluorinated phases. These soft phonon modes indicate weak lattice restoring forces and a tendency for spontaneous structural distortions. This instability is consistent with their pronounced elastic anisotropy, where SiF_2 ($A_1 = 2.38$, $A_2 = 1.16$, $A_3 = 1.36$) and SiF_5 ($A_1 = 1.36$, $A_2 = 1.43$, $A_3 = 2.09$) exhibit strongly direction-dependent bonding and uneven stress distribution. Although these materials show favourable electronic tunability, their combined anisotropic mechanical response and phonon instabilities ultimately undermine structural integrity.

Among all investigated systems, nitrogen doping shows the most

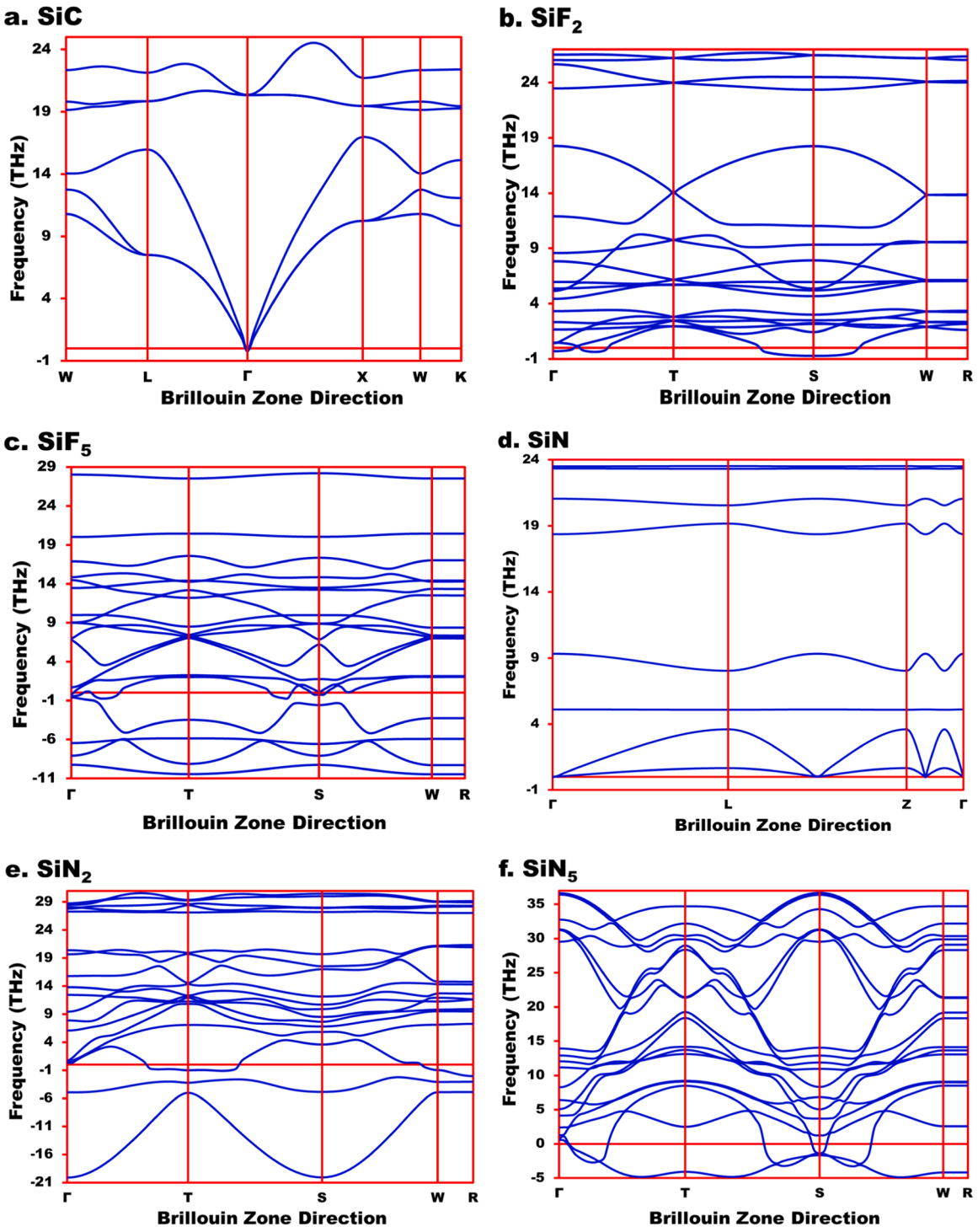

Fig. 12. Phonon dispersion curves of (a) SiC, (b) SiF_2, (c) SiF_5, (d) SiN, (e) SiN_2 and (f) SiN_5.

favourable balance of thermodynamic stability, electronic properties, and mechanical performance. Cluster expansion predicts three stable phases (SiN, SiN_2, and SiN_5) all lying on the DFT ground-state line. SiN exhibits semiconducting behaviour with an indirect band gap of 1.76 eV, while SiN_2 and SiN_5 become semi-metallic due to the increasing contribution of N 2p states crossing the Fermi level, indicating that electronic conductivity can be tuned through composition. Mechanically, SiN_2 satisfies all Born stability criteria and shows high elastic moduli with a Pugh's ratio greater than 1.75, indicating ductility and improved strain accommodation, alongside pronounced anisotropy ($A_1 = 2.31$, $A_2 = 0.96$, $A_3 = 2.27$) that reflects a directionally dependent but relatively balanced mechanical response. However, phonon calculations reveal that only SiN is dynamically stable, whereas SiN_2 and SiN_5 exhibit imaginary phonon modes, indicating lattice instabilities at 0 K. Thus, despite the attractive ductility and conductivity of SiN_2, its vibrational instability may lead to structural distortions under equilibrium conditions. However, SiN emerges as the most robust phase, combining thermodynamic, mechanical, and dynamical stability with moderate anisotropy, making it the most reliable candidate for practical applications.

Overall, the results demonstrate that dopant selection strongly influences the balance between structural stability and electronic

performance in silicon-based materials. Carbon doping produces only one stable compound (SiC), which exhibits strong covalent bonding, a widened band gap, and good dynamical stability, but is mechanically brittle and potentially prone to fracture under lithiation-induced strain. Fluorine doping, although electronically tuneable from semiconducting (SiF_2) to semi-metallic (SiF_5), results in phases that are both mechanically and dynamically unstable due to pronounced elastic anisotropy and phonon softening, limiting their practical applicability. In contrast, nitrogen doping provides the most balanced overall behaviour, with multiple thermodynamically stable phases and tuneable electronic properties. However, only SiN achieves full dynamical, mechanical, and thermodynamic stability, making it the most promising and robust candidate among all investigated systems. Consequently, SiN emerges as the most balanced candidate, offering thermodynamic, mechanical, and vibrational stability together with favourable electronic properties for next-generation silicon-based lithium-ion battery anodes.

6. Conclusion

The cluster expansion analysis of $Si_{1-x}M_x$ (M = C, N, and F) demonstrates that dopant chemistry strongly influences the thermodynamic, electronic, and mechanical properties of silicon-based materials. Accurate cluster expansion models were obtained using the UNCLE code, with cross-validation scores well below the 5 meV/atom threshold, confirming the reliability of the predicted ground-state phases and formation energies.

Carbon, fluorine, and nitrogen doping exhibit distinct effects on the structural, electronic, mechanical, and vibrational properties of silicon. Carbon doping produced predominantly metastable phases, with SiC identified as the only thermodynamically stable compound. SiC adopts a cubic F-43m structure with shortened Si-C bond lengths, a widened band gap, and no imaginary phonon modes, confirming its dynamical stability. Its elastic behaviour shows moderate anisotropy (A = 1.87), reflecting direction-dependent stiffness arising from strong covalent bonding. However, despite its high stiffness, low Pugh's and Poisson's ratios indicate brittle behaviour, suggesting limited resistance to fracture under repeated lithiation-induced strain.

Fluorine doping generated thermodynamically stable phases such as SiF_2 and SiF_5 with negative formation energies and orthorhombic symmetry. SiF_2 exhibited semiconducting behaviour, whereas SiF_5 was semi-metallic. However, both phases displayed imaginary phonon modes, indicating dynamical instability, while SiF_5 also failed to satisfy the Born stability criteria. Both phases exhibit pronounced elastic anisotropy, reflecting strongly direction-dependent bonding and uneven stress distribution. Nitrogen doping provides the most balanced overall behaviour, generating three thermodynamically stable phases (SiN, SiN_2, and SiN_5) with tuneable electronic properties. Although SiN_2 exhibits ductility and strong anisotropy, only SiN is fully dynamically stable, while SiN_2 and SiN_5 display phonon instabilities that limit their practical applicability. Importantly, SiN combines thermodynamic, mechanical, and vibrational stability with moderate anisotropy, indicating a more balanced and structurally robust response under deformation. Dopant selection critically governs the interplay between bonding, anisotropy, and stability, with SiN emerging as the most promising candidate for silicon-based lithium-ion battery anodes due to its optimal combination of stability and performance.

Based on the computational predictions, future experimental work should focus on the synthesis of SiN and SiC using techniques such as chemical vapour deposition, reactive sputtering, or thermal nitridation/carburization. Structural stability can be verified using X-ray diffraction (XRD) and Raman spectroscopy, while X-ray photoelectron spectroscopy (XPS) can be used to investigate chemical bonding. Electrochemical testing, including charge-discharge cycling and impedance spectroscopy, would provide valuable insight into the suitability of these materials as lithium-ion battery anodes and facilitate validation of the present theoretical predictions.

Author contribution

All authors contributed equally.

Declaration of Competing Interest

The authors declare that they have no known competing financial interests or personal relationships that could have appeared to influence the work reported in this paper.

Acknowledgements

We sincerely acknowledge the financial support received from the National Research Foundation (NRF), the Department of Science, Technology and Innovation Energy Storage Research Development Innovation Flagship Programme of South Africa, and the South African National Energy Development Institute (SANEDI) Secretariat. This study was conducted using computational resources provided by the Materials Modelling Centre (MMC) at the University of Limpopo and the Centre for High Performance Computing (CHPC) in Cape Town, South Africa. The calculations have been performed with MedeA UNCLE, using the UNiversal CLuster Expansion (UNCLE) code. We would also like to thank Dr KT Malatji for his helpful simulation insights for the cluster expansion approach.

Appendix A

Stability criteria for cubic symmetry

C_{11}-C_{12}> 0

$C_{11} + 2C_{12}$> 0

C_{44}> 0

Stability criteria for hexagonal symmetry

C_{ii}> 0

C_{11}-C_{12}> 0

$C_{11} + C_{12}$> 0

$C_{33} + 2C_{13} > 0$

Stability criteria for cubic symmetry

$C_{ii} > 0$

$C_{11}C_{22} > C_{12}^2$

$C_{11}C_{22}C_{33} + 2C_{12}C_{13}C_{23} - C_{11}C_{23}^2 - C_{22}C_{13}^2 - C_{33}C_{12}^2 > 0$

Zener anisotropy factor

$$A_1 = \frac{2C_{44}}{C_{11} - C_{12}}$$

$$A_2 = \frac{2C_{44}}{C_{11} + C_{33} - C_{13}}$$

$$A_3 = \frac{C_{44}}{C_{66}}$$

References

[1] J. Mitali, S. Dhinakaran, A.A. Mohamad, Energy storage systems: a review, Energy Storage Sav. 1 (2022) 166–216.
[2] H. Chen, T.N. Cong, W. Yang, C. Tan, Y. Li, Y. Ding, Progress in electrical energy storage system: a critical review, Progress. Nat. Sci. 19 (2009) 291–312.
[3] H. Ibrahim, A. Ilinca, J. Perron, Energy storage systems-characteristics and comparisons, Renew. Sustain. Energy Rev. 12 (2008) 1221–1250.
[4] L. Sun, Y. Liu, R. Shao, J. Wu, R. Jiang, Recent progress and future perspective on practical silicon anode-based lithium-ion batteries, Energy Storage Mater. 46 (2022) 482–502.
[5] Y. Li, Q. Li, J. Chai, Y. Wang, J. Du, Si-based anode lithium-ion batteries: a comprehensive review of recent progress, ACS Mater. Lett. 5 (2023) 2948–2970.
[6] F.Z. Zhang, Y.Y. Ma, M.M. Jiang, W. Luo, J.P. Yang, Boron heteroatom-doped silicon-carbon peanut-like composites enables long life lithium-ion batteries, Rare Met. 41 (2022) 1276–1283.
[7] H. Ou, Y. Peng, X. Sang, H. Zhong, J.E. Zhou, X. Lin, R.C.K. Reddy, G. Ma, Y. Wu, Recent advances in silicon-based composite anodes modified by metal-organic frameworks and their derivatives for lithium-ion battery applications, J. Alloy. Compd. 960 (2023) 170713.
[8] W. Huang, Y. Wang, L. Lv, G. Zhu, Q. Qu, H. Zheng, Solid interfacial conversion based on fluorine-silicon reaction enables, Energy Storage Mater. 60 (2023) 102837.
[9] Y. Li, Q. Li, J. Chai, Y. Wang, J. Du, Z. Chen, Y. Rui, L. Jiang, B. Tang, Si-based anode lithium-ion batteries: a comprehensive review of recent progress, ACS Mater. Lett. 5 (2023) 2948–2970.
[10] J. Miao, B. Wang, C.V. Thompson, First-order amorphous-to-amorphous phase transitions during lithiation of silicon thin films, Phys. Rev. Mater. 4 (2020) 043608.
[11] M. Kim, Z. Yang, I. Bloom, Review—the lithiation/delithiation behavior of si-based electrodes: a connection between electrochemistry and mechanics, J. Electrochem. Soc. 168 (2021) 010523.
[12] M.K.Y. Chan, C. Wolverton, J.P. Greeley, First principles simulations of the electrochemical lithiation and delithiation of faceted crystalline silicon, J. Am. Chem. Soc. 134 (2012) 14362–14374.
[13] A. Nasir, E. Yabalak, Review: Toward high-energy lithium-ion batteries—hybrid carbon architectures with synergistic doping and interface control, Springer (2026), https://doi.org/10.1007/s10853-026-12875-w.
[14] S. Zhi, Q. Dai, H. Wang, D. Wu, L. Zhao, C. Hu, L. Dai, Heteroatom-doped carbon materials for multifunctional noncatalytic applications, ACS Nano 19 (2025) 29860–29897.
[15] R. Shao, F. Zhu, Z. Cao, Z. Zhang, M. Dou, Heteroatom-doped carbon networks enabling robust and flexible silicon anodes for high energy Li-ion batteries, J. Mater. Chem. A 8 (2020) 18338–18347.
[16] H. Dong, J. Wang, H. Ding, F. Zong, P. Wang, R. Song, N. Zhang, X. Cui, X. Cui, S. Li, Exploring the practical applications of silicon anodes: a review of silicon-based composites for lithium-ion batteries, Ionics 28 (2022) 3057–3077.
[17] A. Ulvestad, H.F. Andersen, I.J.T. Jensen, T.T. Mongstad, J.P. Maehlen, O. Prytz, M. Kirkengen, Substoichiometric silicon nitride - an anode material for Li-ion batteries promising high stability and high capacity, Sci. Rep. 8 (2018) 8634.
[18] A.W. Nemaga, S.Y. Lai, T. Nguyen, A. Ulvestad, C.E.L. Foss, Unveiling the advantages of silicon nitride nanoparticle anodes for enhanced cyclic stability, rate performance, and mechanical robustness, ACS Omega 10 (2025) 2608–2615.
[19] M. Wu, G. Cai, Z. Li, L. Ye, C. Wang, Structures and properties of carbon-doped silicon as anode material for lithium ions battery: a first-principles study, Vacuum 225 (2024) 113222.
[20] P. Serp, P. Kalck, R. Feurer, Chemical vapor deposition methods for the controlled preparation of supported catalytic materials, Chem. Rev. 102 (2002) 3085–3128.
[21] D.L. Zhang, Processing of advanced materials using high-energy mechanical milling, Progress. Mater. Sci. 49 (2004) 537–560.
[22] I.S. Kim, G.E. Blomgren, P.N. Kumta, Si-SiC nanocomposite anodes synthesized using high-energy mechanical milling, J. Power Sources 130 (2004) 275–280.
[23] L.P. Yang, Y. Wang, X.Q. Zhao, X.J. Lin, B.B. Zhang, Y.G. Sun, S. Chen, Controlled synthesis of hollow Si-C microspheres and its potential as an anode material in lithium-ion batteries, J. Alloy. Compd. 968 (2023) 171860.
[24] S.A. Hosseini Ravandi, M. Sadrjahani, A. Valipouri, F. Dabirian, F.K. Ko, Recently developed electrospinning methods: a review, Text. Res. J. 92 (2022) 5130–5145.
[25] F. Li, Y. Anjarsari, J. Wang, R. Azzahiidah, J. Jiang, J. Zou, K. Xiang, H. Ma, Arramel, Modulation of the lattice structure of 2D carbon-based materials for improving photo/electric properties, Carbon Lett. 33 (2023) 1321–1331.
[26] Z. Shen, H. Liu, Y. Shen, J. Hu, L. Chen, C. Nan, Machine learning in energy storage materials, Interdiscip. Mater. 1 (2022) 175–195.
[27] Q. Hu, J. Lu, J. Hui, Z. Rao, Y. Ren, H. Wang, Artificial intelligence-driven development in rechargeable battery materials: progress, challenges, and future perspectives, Adv. Funct. Mater. (2025) **35**.
[28] V. Choyal, N. Sagar, G. Sai Gautam, Constructing and evaluating machine-learned interatomic potentials for Li-based disordered rocksalts, J. Chem. Theory Comput. 20 (2024) 4844–4856.
[29] Q. Hu, W. Wang, J. Lu, H. Zhu, Q. Liu, Y. Ren, H. Wang, J. Hui, High-throughput screening of high energy density LiMn1-xFexPO4 via active learning, Chin. Chem. Lett. 36 (2025) 110344.
[30] Z. Sun, X. Li, Y. Wu, Q. Gu, S. Zheng, Machine learning-assisted simulations and predictions for battery interfaces, Adv. Intell. Syst. 7 (2025).
[31] B. Mortazavi, Recent advances in machine learning-assisted multiscale design of energy materials, Adv. Energy Mater. 15 (2025).
[32] B. Madika, A. Saha, C. Kang, B. Buyantogtokh, J. Agar, C.M. Wolverton, P. Voorhees, P. Littlewood, S. Kalinin, S. Hong, Artificial intelligence for materials discovery, development, and optimization, ACS Nano 19 (2025) 27116–27158.
[33] K. Shahzad, A.I. Mardare, A.W. Hassel, Accelerating materials discovery: combinatorial synthesis, high-throughput characterization, and computational advances, Science Technology Advanced Materials Methods 4 (2024).
[34] L. Barroso-Luque, P. Zhong, J.H. Yang, F. Xie, T. Chen, B. Ouyang, G. Ceder, Cluster expansions of multicomponent ionic materials: formalism and methodology, Phys. Rev. B 106 (2022) 144202.
[35] Y.L. Müller, A.R. Natarajan, Constructing multicomponent cluster expansions with machine-learning and chemical embedding, npj Comput. Mater. 11 (2025) 60.
[36] A. Poulia, A.E. Karantzalis, Latest advancements and mechanistic insights into high-entropy alloys: design, properties and applications, Materials 18 (2025) 5616.
[37] M. Ge, C. Cao, G.M. Biesold, C.D. Sewell, S.M. Hao, J. Huang, W. Zhang, Y. Lai, Z. Lin, Recent advances in silicon-based electrodes: from fundamental research toward practical applications, Adv. Mater. 33 (2021) 2004577.
[38] H. Hyrondelle, A. Terry, J. Lhoste, S. Tencé, K. Lemoine, J. Olchowka, D. Dambournet, C. Tassel, J. Gamon, A. Demourgues, Fluorine as a key element in solid-state chemistry of mixed anions 3D transition metal-based materials for electronic properties and energy, Chem. Rev. 125 (2025) 4287–4358.
[39] D. Lerch, O. Wieckhorst, G.L.W. Hart, R.W. Forcade, S. Müller, UNCLE: a code for constructing cluster expansions for arbitrary lattices with minimal user-input, Model. Simul. Mater. Sci. Eng. 17 (2009) 055003.

[40] Q. Wu, B. He, T. Song, J. Gao, S. Shi, Cluster expansion method and its application in computational materials science, Comput. Mater. Sci. 125 (2016) 243–254.
[41] T. Mueller, G. Ceder, Bayesian approach to cluster expansions, Phys. Rev. B - Condens. Matter Mater. Phys. 80 (2009) 024103.
[42] J. Hafner, Ab-initio simulations of materials using VASP: density-functional theory and beyond, J. Comput. Chem. 29 (2008) 2044–2078.
[43] W. Kohn, L.J. Sham, Self-consistent equations including exchange and correlation effects, Phys. Rev. 140 (1965) A1133.
[44] J.P. Perdew, K. Burke, M. Ernzerhof, Generalized gradient approximation made simple, Phys. Rev. Lett. 77 (1996) 3865.
[45] H.J. Monkhorst, J.D. Pack, Special points for Brillouin-zone integrations, Phys. Rev. B 13 (1976) 5188.
[46] K. Parlinski, Z.Q. Li, Y. Kawazoe, First-principles determination of the soft mode in cubic ZrO2, Phys. Rev. Lett. 78 (1997) 4063–4066.
[47] A. Van De Walle, G. Ceder, Automating First-Principles Phase Diagram Calculations, J. Ph. Equil. 23 (2002) 348.
[48] J.P. Barton, E. De Leonardis, A. Coucke, S. Cocco, ACE: Adaptive cluster expansion for maximum entropy graphical model inference, Bioinformatics 32 (2016) 3089–3097.
[49] G.L.W. Hart, V. Blum, M.J. Walorski, A. Zunger, Evolutionary approach for determining first-principles hamiltonians, Nat. Mater. 4 (2005) 391–394.
[50] A. Díaz-Ortiz, R. Drautz, M. Fähnle, H. Dosch, J.M. Sanchez, Structure and magnetism in bcc-based iron-cobalt alloys, Phys. Rev. B - Condens. Matter Mater. Phys. 73 (2006).
[51] S. Muhammady, N.P. Sendi, Y. Kurniawan, Y. Darma, Effect of isotropic pressure on structural and electronic properties of silicon system with Fd-3m space group, J. Phys. Conf. Ser. 1204 (2019) 012117.
[52] C. He, L. Sun, C. Zhang, J. Zhong, Two viable three-dimensional carbon semiconductors with an entirely sp 2 configuration, Phys. Chem. Chem. Phys. 15 (2013) 680–684.
[53] H. Liu, M. Xing, Q. Fan, Novel direct and wide bandgap SiC semiconductors: High-throughput screening and density functional theory, Results Phys. 65 (2024) 107966.
[54] Y. Xing, B. Ren, B. Li, J. Chen, S. Yin, H. Lin, J. Liu, H. Chen, Principles and methods for improving the thermoelectric performance of SiC: a potential high-temperature thermoelectric material, Materials 17 (2024) 3636.
[55] F. Mouhat, F.X. Coudert, Necessary and sufficient elastic stability conditions in various crystal systems, Phys. Rev. B -Condens. Matter Mater. Phys. 90 (2014) 224104.
[56] C.M. Kube, Elastic anisotropy of crystals, AIP Adv. 6 (2016).
[57] R.V. Southwell, Castigliano's principle of minimum strain-energy, Proc. R. Soc. Lond. Ser. A-Math. Phys. Sci. 154 (1936) 4–21.
[58] S.F. Pugh, XCII. Relations between the elastic moduli and the plastic properties of polycrystalline pure metals, Lond. Edinb. Dublin Philos. Mag. J. Sci. 45 (1954) 823–843.
[59] H. Gercek, Poisson's ratio values for rocks, Int. J. Rock. Mech. Min. Sci. 44 (2007) 1–13.